Developing Descriptors To Predict Mechanical Properties of Nanotubes

Tammie L. Borders,*,[†] Alexandre F. Fonseca,[‡] Hengji Zhang,[§] Kyeongjae Cho,[§,∥] and Andrew Rusinko, III[⊥]

[†]Department of Chemistry, University of North Texas, Denton, Texas 76203, United States
[‡]Department of Physics, UNESP - Sao Paulo State University, Bauru, SP, 17033-360, Brazil
[§]Department of Physics, University of Texas at Dallas, Richardson, Texas 75080, United States
[∥]Department of Materials Science and Engineering, University of Texas at Dallas, Richardson, Texas 75080, United States
[⊥]Novartis Institutes of Biomedical Research, Chemistry, Fort Worth, Texas 76134, United States

Ⓢ *Supporting Information*

ABSTRACT: Descriptors and quantitative structure property relationships (QSPR) were investigated for mechanical property prediction of carbon nanotubes (CNTs). 78 molecular dynamics (MD) simulations were carried out, and 20 descriptors were calculated to build quantitative structure property relationships (QSPRs) for Young's modulus and Poisson's ratio in two separate analyses: vacancy only and vacancy plus methyl functionalization. In the first analysis, C_{N2}/C_T (number of non-sp2 hybridized carbons per the total carbons) and chiral angle were identified as critical descriptors for both Young's modulus and Poisson's ratio. Further analysis and literature findings indicate the effect of chiral angle is negligible at larger CNT radii for both properties. Raman spectroscopy can be used to measure C_{N2}/C_T, providing a direct link between experimental and computational results. Poisson's ratio approaches two different limiting values as CNT radii increases: 0.23–0.25 for chiral and armchair CNTs and 0.10 for zigzag CNTs (surface defects <3%). In the second analysis, the critical descriptors were C_{N2}/C_T, chiral angle, and M_N/C_T (number of methyl groups per total carbons). These results imply new types of defects can be represented as a new descriptor in QSPR models. Finally, results are qualified and quantified against experimental data.
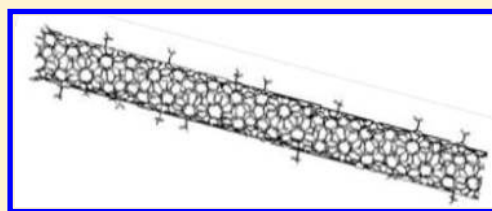
1. INTRODUCTION

Carbon nanotubes (CNTs) have unparalleled mechanical, electronic, and thermal properties.[1,2] With strength and stiffness values of 100 and 1,000 GPa, respectively, CNTs have been used to reinforce polymer, ceramic, and metal matrices for improved stiffness, strength, and toughness.[3−8] There is a large degree of flexibility in tailoring CNTs, which creates a large parameter space that is both computationally and experimentally prohibitive to explore. There are four factors to address for mechanical property optimization in CNT-reinforced composites: aspect ratio, homogeneity of CNT dispersion, interfacial CNT-polymer stress transfer, and CNT alignment.[2,5] Critical aspect ratio is the minimal length to width ratio required to attain maximum load transfer in the polymer matrix.[9] In one study, epoxide functionalized multiwalled CNTs (MWCNTs) realized a critical aspect ratio reduced by a factor of 3.[10] Functionalization is also used to improve CNT dispersion and tailor the CNT-polymer interfacial bonding.[11−16] In MWCNTs, load transfer is improved with interwall bonding.[17−19] Mechanical properties can be modified by these and other codependent variables.

Descriptors and quantitative structure property relationships (QSPRs) are powerful approaches commonly used in drug discovery that have not been explored in CNT-reinforced composites although there has been some work in nano-toxicity.[20−22] In this study, we seek to identify descriptors for mechanical property prediction through QSPR models and evaluate the qualitative and quantitative results against computational and experimental data.[23]

2. COMPUTATIONAL METHODS AND DESCRIPTION OF NANOTUBE SYSTEMS

The adaptive intermolecular reactive empirical bond order (AIREBO) potential was used for molecular dynamics (MD) simulations. It extends the second generation of the reactive empirical bond order (REBO) potential to include torsional and pairwise van der Waals interactions.[24] The REBO potential is well-known to accurately describe carbon−carbon and hydrocarbon molecular short-range interactions when allowing for bond breaking, bond formation, and rehybridization.[25] While in general, the cutoff distance within the REBO code should be modified to correct for overestimation of the maximum carbon−carbon bond breaking force, modifications are unnecessary for this study as it focused solely on the linear elastic region of CNT deformations.[26]

The CNT coordinate system is defined as x and y for the lateral axes and z for the length-wise axis. There were 78 single-walled carbon nanotube (SWCNT) test cases, covering a 10× range of radii, all three chiralities, surface vacancies, surface functionalization, and multiple chiral angles. Pristine SWCNTs of equal length (100 Å) were created with JCrystalSoft Nanotube Modeler version 1.6.1 and individually processed with Python scripts to create four types of surface defects: single vacancy, double vacancy, mixed single and double vacancy, and methyl functionalization. A single vacancy is a single missing atom, a double vacancy is side-by-side missing atoms, and vacancy percent is the surface area covered by the specified type of vacancy. A vertical double defect has an orientation angle of maximum width less than 45 degrees relative to the CNT longitudinal axis. Defect positions were randomly selected, at least 4 Å from the CNT end and with at least 4 Å of separation between two defects.

The tensile strain MD simulations had several steps. First, initial structures were fully relaxed, taking from 150−250 ps dependent on the test case. Next, the outer rings of carbon atoms at both ends of the CNT were each moved 0.1 Å outward increasing the CNT length to 100.2 Å, equivalent to 0.2% tensile strain. Keeping the carbon atoms at the z-axis extremities fixed in place, this structure was fully relaxed at 0 K, which took from 20 to 100 ps dependent on the test case. The iterative process of increasing the length and relaxing the structure was repeated to achieve a total strain of 5%, well within the ∼10% tensile strain failure limit.[27] A time step of 0.5 fs was used, slower than the fastest process (C−H bond stretching) simulated.[27] To integrate Newton's equations of motion, the velocity Verlet method was implemented.[28] The Berendsen thermostat rescaled the velocities of the particles to maintain the simulation temperature.[29] At each step, the total structure energy and geometries were collected.

Young's modulus (Y) is a measure of stiffness defined as the ratio of axial stress (σ) to axial strain (ε) over ranges of stress in which Hooke's law holds true. It was calculated via the second derivative of the strain energy density.[30]

$$\frac{2}{AL_o} E = Ys^2 \tag{1}$$

Symbols are Y as Young's modulus, A as cross-sectional area, L_o as the original relaxed length, ε as the axial strain, and E as the strain energy. The cross-sectional area A is calculated as $2\pi Rh$ (h is the CNT wall thickness equal to 0.34 nm), and R is the CNT radius.[30]

Poisson's ratio (PR) is the negative ratio of the lateral to longitudinal strain as an axial load is applied. For this study, values were calculated at an initial and final strain of 0% and 5%, respectively.

$$PR = -\frac{\text{lateral strain}}{\text{longitudinal strain}} = -\frac{(r_f - r_i)/r_i}{(l_f - l_i)/l_i} \tag{2}$$

Symbols are r_i (l_i) and r_f (l_f) as the radii (length) at the initial and final strain, respectively. The initial and final CNT average radii were calculated using all individual radii in the middle 70% CNT section.

3. DESCRIPTORS AND INFORMATICS METHODS

Chemical descriptors are numerical representations of chemical information; types include topological, geometric, quantum mechanical, etc.[31] Most descriptors to date have been developed for drug design and discovery, primarily focused on small drug-like molecules.[32] While there has been some work on materials descriptors,[33] the field is immature.[34] Much work is needed in descriptor development for nanoparticles, such as to represent waviness or spatial and time distributions of filler particles.[34] Constitutional, topological, and physico-chemical descriptors were used in this study. Deriving a quantitative structure property relationship (QSPR) includes data collection and preprocessing, visualization, descriptor selection, model development, and validation.[35] While this data set is purely computational, adding experimental data and recreating the mathematical models would be straightforward. However, the establishment of a vetting process to create a polymer nanocomposites database has been a challenge to the academic community and reliable experimental data are not readily available.[36] Principal component analysis (PCA) loadings plots were used to identify clusters.[37,38] Descriptor selection is inherent to the mathematical model, partial least-squares regression (PLS), which determines a linear regression model by finding a direction vector in descriptor space that maximizes explained variance in the response.[39] The premise is to reduce dimensionality of the original data set via forming a set of latent variables without loss of essential information. PLS works well for large numbers of variables and addresses descriptor colinearity but interpretability can be a disadvantage.[35,39]

Identification of important, stable descriptors is crucial. Star plots can be used to make qualitative decisions about descriptor importance and robustness over a set of conditions.[40−42] A traditional star plot represents a unique data point and is composed of a sequence of equiangular spokes. Each spoke represents a variable with the spoke length proportional to the magnitude of that variable in that data point.[42] Modifying the definition of the traditional star plot, each star represents a variable, and the spokes are observations of that variable over a set of conditions.[40] Spoke length is proportional to the normalized descriptor strength and provides a measure of descriptor importance. The spoke color indicates the correlation of the descriptor in the model with blue being positive (correlated) and red being negative (anticorrelated).[40] A star plot with large, relatively consistent spoke length and uniform coloring is indicative of a descriptor that is important and stable throughout the model. In Figure 1, stars A and B represent stable descriptors of negative and positive weighting, respectively. Because the relative spoke length in A is larger than B, it is considered to be more important to the model. While star C is of uniform color, it has inconsistent spoke lengths and implies the descriptor might be ill-represented or fitting noise describing weights from highly nonlinear models.[40]
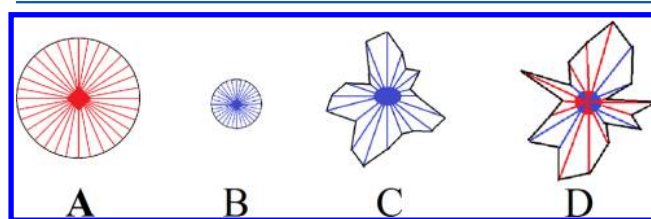

Figure 1. Stars A and B are represent stable descriptors. Star A has a large negative weighting, and star B has a smaller positive weighting. Star C is of uniform color (blue) but inconsistent spoke length and could indicate an unstable descriptor. Star D is of widely varying color and spoke length, definitely an unstable descriptor.

Star D oscillates in color and has nonuniform spoke length, clearly indicating an unstable descriptor. Star plots are used to look at consistency in data, uniform spoke length, and color. The least-squares constraint can easily mask an otherwise straightforward interpretation, especially for nonorthogonal features. Direct interpretation of correlation from star plots is generally avoided.

4. RESULTS AND DISCUSSION

The goals of the study are to identify descriptors that can be used to predict the mechanical properties Young's modulus and Poisson's ratio. The first analysis uses a vacancy only test set, and the second uses a vacancy and methyl functionalization test set. The computational results are compared to each other and quantified against experimental results. The 20 CNT descriptors evaluated in the study are defined in Table 1. The full data set is provided as Supporting Information.

Table 1. Twenty Original Set of Descriptors, Each One's Abbreviation Used in the Data Tables and Definitions Are Provided[a]

	descriptors	symbol	definition
1	area	A	cross-sectional area of nanotube ($Å^2$)
2	chiral angle	CA	chiral angle (radians)
3	average radius	R_A	average of first three end rings radii for relaxed CNT (Å)
4	theoretical radius	R_T	theoretical radius of perfect nanotube (Å)
5	aspect ratio	AR	ratio of the length to the diameter
6	% single defects	$\%_{SD}$	percentage of single defects
7	% double defects	$\%_{DD}$	percentage of double defects
8	% methyl groups	$\%_M$	percentage of surface functionalized methyl groups
9	# missing C's	C_M	number of missing due to a vacancy defect
10	# methyl groups	M_N	number of methyl functional groups
11	# total C's	C_T	total number of carbons in the test case
12	M_N/C_T	M_N/C_T	ratio of methyl groups to total number of carbons
13	C_M/C_T	C_M/C_T	ratio of missing carbons to total number of carbons
14	# single defects	$\#_{SD}$	number of single defect types
15	# double defects	$\#_{DD}$	number of double defect types
16	# nonsp² C's	C_{N2}	number of nonsp² hybridized carbons
17	C_{N2}/C_T	C_{N2}/C_T	ratio of nonsp² hybridized carbons to total number of carbons
18	surface area	S_P	total surface area of nanotube (uses average radius)
19	defect surface area	S_D	surface area of defects
20	S_D/S_P	S_D/S_P	ratio of defect area to total surface area

[a]Simple descriptors including fragment counts and surface areas were used.

4.1. Analysis 1 - Vacancy Only Test Set. Values of Young's modulus vary widely in the literature. For pristine CNTs, Young's modulus was calculated as 1.47, 1.10, and 0.726 TPa for (10,0), (8,4), and (10,10) SWCNTs, respectively.[43] It was experimentally calculated as 0.9 to 1.9 TPa,[44] while one ab initio result yielded 0.5 to 1.1 TPa (radii between 3 and 7 Å).[45] Select MD results are on the order of 1 TPa.[4,46] Several studies

have addressed vacancy-laden CNTs; one study found reduction of Young's modulus to be virtually independent with 3−24% vacancies (temperatures less than 300 K) while another found a 15% reduction for 1.4% surface vacancies.[47−50] Experimental and computational studies conclude that vacancies lead to a decrease in Young's modulus, but the quantitative model varies.[47,50−52] Reasons for variation include dependence (or independence) on chirality and diameter, differing values used for the wall thickness,[53] variation in procedural methods,[54] and variation of computational methods. With respect to vacancies, there is much variation in the number, type, and distribution. The data set for this study is generated by a single computational method, employs the same procedural method across all cases, assumes a wall thickness of 0.34 nm,[54] and evaluates effects of CNT chirality and diameter, vacancy type, size, and distribution.

Values for Poisson's ratio also have a large distribution in the literature. One DFT study predicted values between 0.11 and 0.19,[45] while two MD results calculated 0.13−0.19[54−56] and another 0.32−0.36.[49] Analytical models proposed values of 0.21 and 0.277−0.280.[57,58] Tight-binding MD found Poisson's ratios of 0.285 and 0.287.[59,60] Other results include an ab initio rendered 0.32[43] and a finite element prediction of 0.31−0.35.[61] A recent paper reported finding variations from 0.06 to 1.414 and concluded accurate prediction Poisson's ratio for single walled CNTs is still an unsolved issue.[62]

The procedure to identify the minimal set of critical descriptors is as follows. With all 20 descriptors as inputs, PLS models were evaluated in parallel with star plot analyses and loadings plot to identify both the categories and most important descriptors. Smaller sets of the 2 and 3 most important descriptors were compared to the 20 descriptor set results, assessing relative accuracy and interpretability. Each model was trained with 80% of the data and 20% used as an external test. The training and testing correlation coefficients, R^2_{Train} and R^2_{Test}, provided a measure of accuracy and predictive power, while Y-scrambling appraised model robustness.[35,63]

The loadings plot (Figure 2) identifies 3 descriptor categories: measure of size, chirality, and number or type of defects. There appear to be three separate clusters for measure of defects, but star plot results for $\#_{DD}$ and $\%_{DD}$ resemble star D in Figure 1 with widely varying color and spoke length, indicating instability. The other two measures of defect clusters fall in the upper right quadrant very close to each other and are considered a single category. The first and second principal components (PC1, PC2) account for 79% of the variance. From Figure 2, the strongest descriptors are C_{N2}/C_T, C_M/C_T, and S_D/S_P, which are all highly correlated with PC1 coefficients of ∼0.25 and PC2 coefficients of ∼0.35.

Table 2 shows the results for the 20-descriptor and 3-descriptor QSPRs. Descriptors listed are those required to capture 85% of model variance, but for test sets 1, 2, and 3A, all 20 descriptors were included in the QSPR. Analytical predictions of properties have shown more complex variation at radii less than ∼2 nm; thus, data were partitioned into 3 different ranges of radii.[64,65] Comparing test sets 1 and 3A to test set 2 indicates a sensitivity to size effects for Young's modulus. The R^2_{Test} values were much lower (0.98 vs 0.75), and 4 descriptors, rather than 3, were selected. For Poisson's ratio, test sets 1 and 3A both required 5 descriptors, whereas only 3 descriptors were necessary for test set 2 but R^2_{Test} values increased slightly. This implies Poisson's ratio is also sensitive to size effects at small radii but less pronounced than for
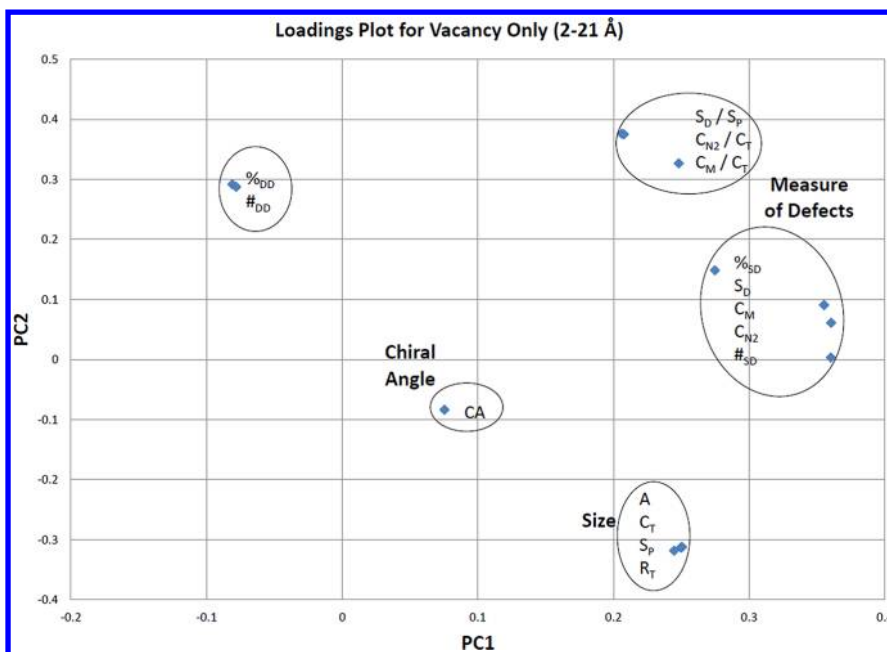
Figure 2. In the vacancy only loadings plot, the categories of size and chiral angle can be seen. There seems to be 3 groupings of defect types but most fall in the upper right quadrant and are considered a single category. The strongest descriptors in both the first and second principal components are C_{N2}/C_T, C_M/C_T, and S_D/S_P, which are all highly correlated.

Table 2. In the Vacancy-Only Analysis, Data Are Divided into Three Sets To Isolate Size Effects[a]

test set	range of radii (Å)	Young's modulus			Poisson's ratio		
		R^2_{Train}	R^2_{Test}	descriptors	R^2_{Train}	R^2_{Test}	descriptors
1	2−7	0.93	0.75	surface area (S_P) chiral angle C_{N2}/C_T % double defects	0.89	0.91	surface area (S_P) chiral angle C_M % double defects % single defects
2	7−21	0.97	0.98	surface area (S_P) chiral angle C_M/C_T	0.93	0.79	surface area (S_P) chiral angle C_M
3A	2−21	0.95	0.76	surface area (S_P) chiral angle C_{N2}/C_T % double defects	0.88	0.91	surface area (S_P) chiral angle C_M/C_T % single defects % double defects
3B	2−21	0.94	0.85	theoretical radius chiral angle C_{N2}/C_T	0.85	0.94	theoretical radius chiral angle C_M/C_T

[a]All 20 descriptors are used in the PLS-based QSPR, but only the ones required to capture 85% of model variance are listed in the table. For Young's modulus, it is clear that there is sensitivity to small size effects (less than 7 Å) by comparing sets 1 and 3A to set 2. The sensitivity to small size effects for Poisson's ratio is less pronounced but follows a similar trend. For both properties, descriptors fell into one of three categories, a) measure of CNT size, b) measure of chirality, and c) measure of number or size of defects. The 3-descriptor model is shown in row 4. Compared to the 20-descriptor model (row 3), interpretability is improved, while cost to accuracy is quite slight.

Table 3. Test Set 3C Removes Radii and Creates a 2-Descriptor QSPR[a]

property	test set	range of radii (Å)	R^2_{Train}	descriptors, individual coefficients			
				chiral angle	individual R^2	measure of defects	individual R^2
Young's modulus	3C	2−21	0.92	chiral angle	0.25	C_{N2}/C_T	0.66
	3C	2−21	0.89	chiral angle	0.25	C_M/C_T	0.63
Poisson's ratio	3C	2−21	0.85	chiral angle	0.68	C_{N2}/C_T	0.16
	3C	2−21	0.87	chiral angle	0.69	C_M/C_T	0.17

[a]Compared to test set 3B in Table 2, cost to accuracy for the Young's modulus model is negligible with C_{N2}/C_T and slight with C_M/C_T. For Poisson's ratio, cost to accuracy is negligible with either descriptor C_{N2}/C_T or C_M/C_T (rows 3 and 4). Assessing the individual coefficients of determination for chiral angle and C_{N2}/C_T (or C_M/C_T) reveals that C_{N2}/C_T captures almost three times the model variance than chiral angle for Young's modulus, while the reverse is true for Poisson's ratio where chiral angle captures approximately three times the model variance.

Young's modulus. The descriptors surface area (S_P) and chiral angle were common to all the models. Several measure-of-defect descriptors were selected. For Young's modulus, C_{N2}/C_T was more common, while C_M or C_M/C_T was used in Poisson's ratio models, implying Poisson's ratio is sensitive to overall defect size whereas Young's modulus is sensitive to both size and type. Using only a single descriptor per category will improve model interpretability, but cost to accuracy must be

assessed. From Figure 2, both surface area (S_P) and radius (R_T) fall in the size category and have very similar coefficients in PC1 and PC2; thus, we can replace S_P with R_T to improve interpretability. C_{N2}/C_T and C_M/C_T are the strongest descriptors in both PC1 and PC2 (Figure 2), $\%_{SD}$ has very similar coefficients to them and $\%_{DD}$ was identified as unstable. Star plots for both properties are consistent in spoke length and color (red or anticorrelated for C_{N2}/C_T for Young's modulus,
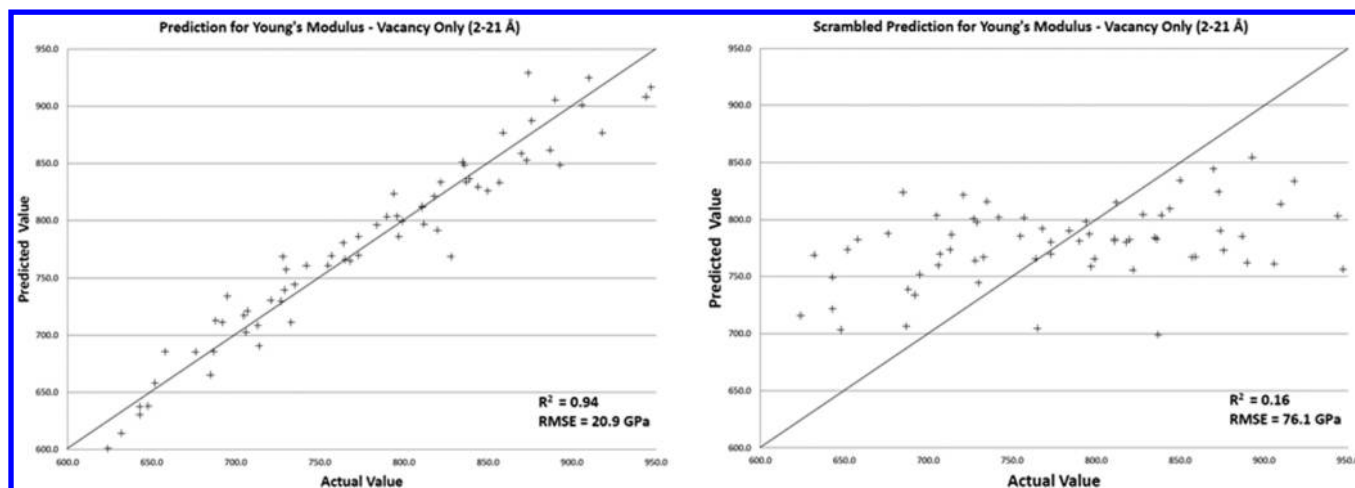
Figure 3. y-Scrambling provides a measure of robustness and was implemented for all analyses. Test set 3A (r = 2−21 Å) predicting Young's modulus using all descriptors is provided as an example.

Table 4. Multiple Linear Regression Coefficients for Vacancy-Only Analysis of Poisson's Ratio ($r \leq 12$ Å; $r > 12$ Å) Support That Dependence on Chiral Angle Decreases with Increasing Radii Size

property	range of radii (Å)	descriptor coefficient	descriptor	descriptor coefficient	descriptor	Y-intercept (GPa)
Poisson's ratio	2−12	0.273	chiral angle	1.06	C_{N2}/C_T	0.08
Poisson's ratio	12−21	0.104	chiral angle	0.16	C_{N2}/C_T	0.19

blue or correlated for C_M/C_T for Poisson's ratio). Thus, it is reasonable to select C_{N2}/C_T for Young's modulus and C_M/C_T for Poisson's ratio. Comparing results for test set 3B to test set 3A, cost to accuracy is slight or negligible.

Size is captured in the denominator of both C_{N2}/C_T and C_M/C_T; thus, it should be possible to remove R_T from the model. Accurate radii measurements are obtainable only through tedious analysis of SEM or TEM images.[66] The use of either C_{N2}/C_T or C_M/C_T was assessed for both mechanical properties, because it would be advantageous to have a common set of descriptors. Results of the 2 descriptor QSPR are shown in Table 3. For Young's modulus, the 2- and 3-descriptor R^2_{Train} values are 0.92 and 0.94, respectively, indicating R_T can be removed from the model. Replacing C_{N2}/C_T with C_M/C_T had a slight cost to accuracy with delta R^2_{Train} of 0.03. For Poisson's ratio, the 2- and 3-descriptor R^2_{Train} values are 0.87 and 0.85, again implying R_T can be removed. Replacing C_M/C_T with C_{N2}/C_T had a negligible effect on accuracy (delta R^2_{Train} of 0.02). The individual coefficients of determination (R^2) for chiral angle and C_{N2}/C_T (or C_M/C_T) account for 90% variance with C_{N2}/C_T capturing the bulk for Young's modulus and chiral angle the majority for Poisson's ratio.

To verify model robustness, y-scrambling was used.[35] Robustness is a signal processing term used to describe approaches that are not significantly degraded when standard operating conditions change. When one begins with a large number of hard-to-control variables, it is likely that some variables will be selected by chance and y-scrambling tests for this. The output y values are scrambled, and the correlation coefficient is calculated. The y-scrambled R^2 value is compared to the R^2 values of the QSPR model. If the R^2 values are similar, the model is not robust. y-Scrambling was used to test robustness for all analyses (example presented in Figure 3). For this example, the R^2 values are 0.16 for the y-scrambling result and 0.95 for the model, which is very desirable for robustness.

Chiral angle accounts for approximately 25% of model variance in test set 3C (2−21 Å) for Young's modulus, but the contribution decreases about 3% from test set 1 (2−7 Å) to test set 2 (7−21 Å) and many Young's modulus studies report chiral independence greater than ∼20 Å.[58,64,65,67−69] While chiral angle accounts for 75% of model variance for Poisson's ratio, the coefficients of chiral angle in a multiple linear regression (MLR) model decrease rapidly (0.273−0.104) between test sets of 2−12 Å and 12−21 Å, as shown in Table 4. This implies Poisson's ratio could be an independent value for large CNTs of specified chirality. Poisson's ratio values for 0% and 3% surface vacancies were calculated for larger CNTs. The (30,30) armchair CNT (radius = 20.6 Å) values ranged from 0.245 to 0.247, (27,16) chiral CNT (radius = 14.9 Å) from 0.225 to 0.251, and (60,0) zigzag CNT (radius = 23.3 Å) from 0.1−0.11. From these data, armchair and chiral CNTs have a Poisson's ratio of ∼0.23−0.25, while zigzag CNTs would be ∼0.10 (with surface vacancies less than 3%). Based on this information, it is reasonable to assume chiral angle is not a factor for Young's modulus for larger CNTs. For experimentally produced CNT forests of mixed chiralities, it also seems reasonable that Poisson's ratio approaches an average composite value. Individual CNT chirality is tedious to measure, via scanning tunneling microscopy or electron diffraction, but C_{N2}/C_T measurements should be attainable through Raman spectroscopy, providing direct correlation between experimental and computational results.[70−74]

4.2. Analysis 2 − Vacancy and Methyl Functionalization Test Set. The test set for analysis 2 covers a range of radii from 3.5 to 7 Å, includes multiple types and sizes of vacancies and sizes of methyl functionalization and has multiple chiralities.

Study of the effect of functional groups on CNT Young's modulus is sparse in the literature. Zhang et al. reasoned there was little effect on moduli unless functionalization exceeded 10%.[75] Another result identified 10% functionalization as the
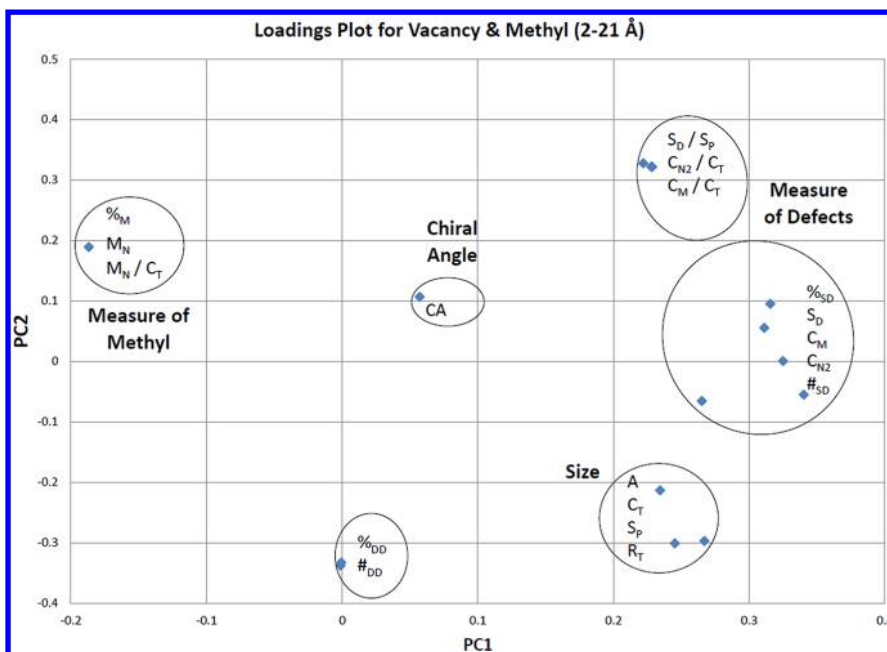
Figure 4. In the vacancy plus methyl only loadings plot, an additional category representing methyl functionalization is clearly seen. The strongest descriptors in both the first and second principal components are from the highly correlated C_{N2}/C_T, C_M/C_T, and S_D/S_P group in the upper right and the highly correlated variables in the upper left representing methyl functionalization.

Table 5. In the Vacancy Plus Functional Group Analysis To Predict Young's Modulus, CNTs with Radii Range from 3.5 to 7 Å Were Used[a]

	Young's modulus			Poisson's ratio		
model	R^2_{Train}	R^2_{Test}	descriptors	R^2_{Train}	R^2_{Test}	descriptors
20-descriptor QSPR	0.95	0.89	surface area (S_p) chiral angle # single defects % double defects C_{N2}/C_T % methyl	0.87	0.81	surface area (S_p) chiral angle S_D % double defects M_N/C_T
3-descriptor QSPR	0.92	0.93	chiral angle C_{N2}/C_T M_N/C_T	0.91	0.81	chiral angle C_{N2}/C_T M_N/C_T

[a]The descriptor categories were the same as the vacancy-only analysis with an additional category for methyl functionalization. In the first row, all 20 descriptors are used in the PLS-based QSPR, but only the ones required to capture 85% of model variance are listed. The selected descriptors were almost identical to the vacancy-only analysis for both properties. The 3-descriptor model has only a slight decrement to accuracy for Young's modulus and a slight improvement for Poisson's ratio.

optimal balance point between decrement of Young's modulus and increase in load transfer between CNT and a polymer matrix.[76] In armchair CNTs, 7.5% and 12% vinyl functionalization produced 10% and 15% decrements in Young's moduli, respectively.[77] Two other studies quantified moduli increases with ~1.5% alkyl functional groups, noting that while the alkyl surface groups degrade the sp^2 hybridization of the CNT, the slight electron donating effect is beneficial to Young's modulus.[77,78]

Literature results analyzing the effect of functionalization on Poisson's ratio are extremely sparse. Coto et al. reported Poisson's ratio decreases from 0.25 to 0.2 with 10% surface functionalization of carboxylic groups but increased with surface vacancies.[79] Methyl functionalization rendered a very slight increase for zigzag (10,0), no change for armchair (5,5), a slight decrease for chiral (8,3), and a decrease for the larger (10,10) armchair CNT.

The loadings plot, using the entire data set of 2−21 Å (Figure 4), identifies four descriptor categories with the first three the same as the vacancy only analysis: size, measure of chirality, measure of defect size, and measure of methyl functionalization. The $\#_{DD}$ and $\%_{DD}$ descriptors shifted positions, confirming the instability identified through earlier

star plot analysis. The first and second principal components (PC1, PC2) account for 69% of data variance. The strongest descriptors are again from the C_{N2}/C_T, C_M/C_T, and S_D/S_P correlated group, with PC1 and PC2 coefficients of ~0.25 and ~0.3, respectively. The three methyl functionalization descriptors are highly correlated and the second strongest with coefficients of ~0.2 in both PC1 and PC2. The formation of a new cluster for a new type of defect is a good indication that different types of defects can be represented by a unique descriptor in a QSPR model.

Table 5 displays the results of the 20-descriptor and 3-descriptor QSPRs for both mechanical properties. The descriptors capturing 85% of the variance in the 20-descriptor model were almost identical to the vacancy only analysis (Table 2). Further, R^2_{Test} and R^2_{Train} values are very similar. These results are favorable that the descriptors found in analysis 1 for vacancy only can be extended to analysis 2 with an additional descriptor added for methyl functionalization, M_N/C_T. Comparing the results for the 20- and 3-descriptor models, there is a slight decrement in R^2_{Train} (0.95−0.92) for Young's modulus but an improvement (0.87 to 0.91) for Poisson's ratio, and these results are on par with accuracies found for analysis 1. The combined results of the loadings plot and model building

Table 6. Experimental Results of Nonirradiated Multiwalled CNTs Are Shown in Rows 1 and 2 and Irradiated Results Are Presented in Rows 3 and 4[a]

sample	gauge length (nm)	inner diameter (nm)	outer diameter (nm)	broken shells	total shells	C_{N2}/C_T (all single vacancies)	C_{N2}/C_T (all methyl groups)	Young's modulus (GPa)
1	1,852	-	14.72	1	12	-	-	990
2	2,024	-	15.71	1	17	-	-	1,049
3	2,105	-	25.97	1	2 or 3	-	-	1,105
4	1,035	37.44	39.48	3	18	0.0002622	0.0000874	932

[a]Sample numbers correspond to the original paper.

are favorable that additive results of vacancy only and methyl functionalization only studies could be used to model a more complex simulation of combined vacancy and methyl functionalization.

M_N/C_T and C_{N2}/C_T can capture the effect of any type of surface vacancy or functionalization by representing delta property due to CNT surface structure change (C_{N2}/C_T) and delta property due to the presence of the surface group itself (M_N/C_T). Models with only methyl functionalization would require both M_N/C_T and C_{N2}/C_T. For example, a single vacancy creates a surface change of three nonsp^2 hybridized carbons, a double defect has four, and a methyl group has a single nonsp^2 hybridized carbon. The methyl group also provides a slight electron donating effect as well as steric hindrance. For other types of functional groups, a scale factor could be developed, based on the distortion to the CNT surface structure change and the electron donating/withdrawing and steric hindrance properties. This implies a single QSPR can be extended to multiple surface defect types, but investigation of more types of functional groups is necessary to fully reach that conclusion. Kuang et al. identified a similar functional form for delta energy with vinyl groups: $\Delta E = (-ax^2 + bx)*$(energy of pristine CNT), where x is proportional to M_N/C_T.[77] For small percent surface functionalization, delta energy increases (bx > ax^2) but as percent functionalization increases, the delta energy decreases (ax^2 > bx). Namilae et al. compared functionalizing a (10,10) CNT with multiple alkyl groups — C_2H_3, C_3H_5, C_4H_7, C_5H_9, all at about 1% density but distributed about the central region.[78] A high strain rate was used possibly producing anomalous results; however, it is the trends between the alkyl groups that are of interest.[27] The results predicted an increase in stiffness of about 0.1% for each additional carbon, which could easily be built into an alkyl scale factor.[78]

4.3. Comparison to Experimental Data. A thorough search of the literature did not find experimental SWCNT data with well characterized surface vacancies or functional groups. Instead, three separate test cases will be evaluated: SWCNTs in a composite, understanding behavior of MWCNTs and predicting properties of monolayer graphene oxide. Multiple linear regression (MLR) coefficients were calculated (eq 3) using both the vacancy and vacancy plus methyl group test sets to derive an expression for predicting change in Young's modulus. It is assumed that chiral angle can be omitted.

$$\Delta(\text{Young's modulus}) = -2225 C_{N2}/C_T + 1975 M_N/C_T \tag{3}$$

The objective of the first study is to provide a first-order explanation for the differences in effective moduli measurements of SWCNTs in a composite. Using stress-induced Raman band shifts, Deng devised a self-consistent method to measure the effective moduli of SWCNT reinforcement in poly vinyl alcohol composites.[80] The SWCNTs were synthesized by

high pressure carbon monoxide (HiPco), a growth method known to have a high defect density.[81] HiPco-produced SWCNTs are 90% pure with an average diameter of 1.1 nm.[82] Chemical oxidative processes are used to remove impurities but are known to change the surface structure of nanotubes.[81] Three effective Young's moduli measurements were taken — 530, 600, and 700 GPa.[80] The author states SWCNT bundling and finite length effects reduce the moduli compared to the theoretical value of 1,000 GPa. We, however, seek to provide insight into the variation between measurements based on SWCNT surface differences. A delta of 170 GPa corresponds to a delta of 0.0764 in C_{N2}/C_T. A single defect has 3 C_{N2} per defect and a double has 4 C_{N2} per defect. This calculates to a delta of 2.5 more single or 1.9 more double defects per 100 carbon atoms in the 530 GPa versus the 700 GPa sample. Given the variation across growth and purification processes, these values are realistic.[81]

The objective of the second study is to provide insight into load transfer mechanism in MWCNTs. Experimental data are shown in Table 6.[17] Young's modulus is provided in eq 4; F is force, A is area, Δl is change in length, and l_o is the original relaxed length.

$$Y = \frac{\sigma}{\varepsilon} = \frac{\frac{F}{A}}{\frac{\Delta l}{l_o}} \tag{4}$$

As the MWCNTs are irradiated, load transfer increases but Young's modulus decreases. For sample 4, the load increase was a factor of 2.4, and the maximum load increase was a factor of 3.[17] The inner CNT area is approximately 95% the area of the outer CNT; for this analysis, we assume that difference to be negligible. A nonirradiated CNT equivalent to sample 4 has a Young's modulus ∼1,050 GPa, which was calculated as the average of samples 1−3 and denoted as YM_o. The irradiated sample 4 Young's modulus is ∼90% YM_o. To achieve a load transfer factor of 2.4 and a Young's modulus of 90% YM_o, two potential explanations are provided. First, assume the walls all participate equally and load transfer is simultaneous across all three walls. Since all walls are assumed to have the same area and $\Delta l/l_o$ is constant, the force per wall is 0.9 times the force on the equivalent, nonirradiated sample (F_o). This means that 0.0002622 C_{N2}/C_T would have to contribute to a ∼10% decrement in Young's modulus. Using eq 3, the decrement to Young's modulus is effectively zero. To achieve a 10% decrement, C_{N2}/C_T would have to be increased by a factor of 100, a large discrepancy between computational and experimental models. The second explanation assumes no decrement to Young's modulus and that the load is not distributed equally across all three walls but on the order of $1*F_o$, $0.8*F_o$, and $0.6*F_o$ for the outer, middle, and inner walls, respectively (the actual numbers are not critical, so long as they add to 2.4, the known increase in load fraction). Calculating Young's modulus

yields a value ~80% of YM_o (~$2.4F_o/3A_o$), not 90% of YM_o as measured. From Figure 5a in Peng's paper, load transfer fraction increases to about 80% of the maximum over the first 2% strain (for defect densities 1−2 orders of magnitude larger than sample 4).[17] It is proposed that the inner walls do not start participating in load transfer until 2% strain or later, also observed computationally.[18] Calculating Young's modulus over 0−5% strain would inflate the composite MWCNT modulus value; in fact, according to Figure 3 in the referenced paper, it is notable that the slope from 0 to 2% is slightly larger than 2−4%.[17] Assuming only the first wall participates for the first 2% strain and all three participate from 2 to 4% strain yields a 0−4% Young's modulus value of ~941 GPa ((1050 + 832)/2), on par with experimental observations making the second explanation more plausible.

The third study predicts the mechanical properties of monolayer graphene oxide. Monolayer graphene is the 2-dimensional (2D) cousin of a nanotube with similar elastic properties.[45] As a 2D material, its strain energy density is normalized by area rather than volume. Mechanical elastic moduli is described by the elastic constant E^{2D} with units of force/length (E^{2D} = volumetric Young's modulus * thickness). Experimentally, monolayer graphene E^{2D} was reported as 342 N/m +- 30 N/m.[83] Monolayer graphene oxide E^{2D} was measured as 145.3 +- 16.3 N/m.[84] Computationally, E^{2D} values of graphene and graphene oxide were calculated to be 382 N/m and 212 N/m, respectively.[85] To use eq 3 to calculate E^{2D} of graphene oxide, values must be multiplied by thickness (0.34 nm) of the graphene sheet. The atomic structure was experimentally determined to be ~40% sp^3 bonding with a oxygen/carbon ratio of 1:5, corresponding to $C_{N2}/C_T \sim 0.4$ and $M_N/C_T \sim 1/6$.[86] Graphene oxide is functionalized by epoxide and hydroxyl groups, but we will use the methyl descriptor as a first-order approximation. Equation 3 predicts $E^{2D} \sim 150$ N/m for graphene oxide, remarkably close to the experimental value of 145 N/m.

5. CONCLUSION

Carbon nanotubes (CNTs) have outstanding physical properties and are considered to be the ultimate reinforcement material in composites.[3,8] There is a large degree of flexibility in tailoring CNTs, creating a large parameter space that is both computationally and experimentally prohibitive to explore. The main goal of the study was to evaluate the potential to use descriptors and QSPRs for predicting Young's modulus and Poisson's ratio in test sets with large variation across radii, chiralities, and number and type of surface defects. The first analysis used a vacancy defect only test set, and the second used a combined vacancy and methyl surface functionalization defect test set. The computational results were analyzed, compared to each other, and quantified against experimental results.

In analysis 1, C_{N2}/C_T and chiral angle were identified as critical descriptors for both Young's modulus and Poisson's ratio. For our test set, chiral angle accounted for ~25% of model variance for Young's modulus, but further analysis combined with literature findings implied the effect of chiral angle on Young's modulus becomes negligible with increase in CNT radii, as those typically produced experimentally. Raman spectroscopy can be used to measure C_{N2}/C_T, providing a direct link between experimental and computational results.[73,74,87] Poisson's ratio approaches two different limiting values as CNT radii increases −0.23−0.25 for chiral and armchair CNTs and 0.10 for zigzag CNTs. Procedurally, PCA

loadings plot were used to identify descriptor categories, correlated descriptors, and the strongest descriptors. Star plots looked at consistency in data; $\#_{DD}$ and $\%_{DD}$ formed a separate cluster on the loadings plot, but star plots indicated instability because of widely fluctuating color and spoke length. Poisson's ratio was more sensitive to size (C_M/C_T) of defect, while Young's modulus was more sensitive to both type and size (C_{N2}/C_T). However, the loadings plot revealed a high degree of correlation between the two descriptors. Using models with either C_{N2}/C_T or C_M/C_T to predict both Young's modulus and Poisson's ratio were of comparable accuracies.

In analysis 2, the critical descriptors were C_{N2}/C_T, chiral angle, and M_N/C_T. Results indicated that new types of defects can be captured in a new descriptor in QSPR models, implying that complex simulations of multiple defect types can be broken down into a set of simpler simulations that will provide comparable results. Procedurally, the loadings plot identified a new cluster for methyl functionalization as the second strongest descriptor set in both the first and second principal component. It was proposed that M_N/C_T and C_{N2}/C_T can capture the effect of any type of surface vacancy or functionalization by representing delta property due to CNT surface structure change (C_{N2}/C_T) and delta property due to the presence of the surface group itself (M_N/C_T) and that a scale factor could be developed for other types of functional groups.

The computational model was qualified and quantified against 3 separate sets of experimental data. First, it was used to provide a first-order explanation of variance for effective Young's modulus of SWCNTs in a composite. Second, it was used to select between two plausible explanations for behavior in irradiated MWCNTs, providing some insight into mechanism. Third, the model was used to directly predict E^{2D} of monolayer graphene oxide and compared to both experimental and computational values.

Computational models are good for qualitative explanations, but refining and verifying those models with experimental data is required to provide a quantitatively accurate answer. Using descriptors that can be easily updated with experimental information in QSPRs is a straightforward approach to achieve this goal.

■ ASSOCIATED CONTENT

ⓈSupporting Information
Input and output data tables. This material is available free of charge via the Internet at http://pubs.acs.org.

■ AUTHOR INFORMATION

Corresponding Author
*E-mail: tammie.l.borders@gmail.com.
Notes
The authors declare no competing financial interest.

■ ACKNOWLEDGMENTS

■ REFERENCES

(1) Endo, M.; Strano, M. S.; Ajayan, P. M. Potential applications of carbon nanotubes. In *Carbon Nanotubes*; Springer-Verlag Berlin: Berlin, 2008; Vol. *111*, pp 13−61.
(2) Coleman, J. N.; Khan, U.; Blau, W. J.; Gun'ko, Y. K. Small but strong: A review of the mechanical properties of carbon nanotube-polymer composites. *Carbon* **2006**, *44* (9), 1624−1652.

(3) Baughman, R. H.; Zakhidov, A. A.; de Heer, W. A. Carbon nanotubes–the route toward applications. *Science* **2002**, *297* (5582), 787−792.

(4) Ogata, S.; Shibutani, Y. Ideal tensile strength and band gap of single-walled carbon nanotubes. *Phys. Rev. B* **2003**, *68* (16), 165409.

(5) Chou, T.-W.; Gao, L.; Thostenson, E. T.; Zhang, Z.; Byun, J.-H. An assessment of the science and technology of carbon nanotube-based fibers and composites. *Compos. Sci. Technol.* **2010**, *70* (1), 1−19.

(6) Breuer, O.; Sundararaj, U. Big returns from small fibers: A review of polymer/carbon nanotube composites. *Polym. Compos.* **2004**, *25* (6), 630−645.

(7) Thostenson, E. T.; Li, C.; Chou, T.-W. Nanocomposites in context. *Compos. Sci. Technol.* **2005**, *65* (3−4), 491−516.

(8) Schadler, L. S.; Giannaris, S. C.; Ajayan, P. M. Load transfer in carbon nanotube epoxy composites. *Appl. Phys. Lett.* **1998**, *73* (26), 3842−3844.

(9) Agarwal, B. D.; Broutman, L. J.; Chandrashekhara, K. *Analysis and Performance of Fiber Composites*, 3rd ed.; Wiley: 2006; p 560.

(10) Duncan, R. K.; Chen, X. G.; Bult, J. B.; Brinson, L. C.; Schadler, L. S. Measurement of the critical aspect ratio and interfacial shear strength in MWNT/polymer composites. *Compos. Sci. Technol.* **2010**, *70* (4), 599−605.

(11) Spitalsky, Z.; Tasis, D.; Papagelis, K.; Galiotis, C. Carbon nanotube-polymer composites: Chemistry, processing, mechanical and electrical properties. *Prog. Polym. Sci.* **2010**, *35* (3), 357−401.

(12) Lin, Y.; Meziani, M. J.; Sun, P. Functionalized carbon nanotubes for polymeric nanocomposites. *J. Mater. Chem.* **2007**, *17* (12), 1143−1148.

(13) Xie, X.-L.; Mai, Y.-W.; Zhou, X.-P. Dispersion and alignment of carbon nanotubes in polymer matrix: A review. *Mater. Sci. Eng., R* **2005**, *49* (4), 89−112.

(14) Barber, A. H.; Cohen, S. R.; Wagner, H. D. Measurement of carbon nanotube polymer interfacial strength. In *Applied Physics Letters*; American Institute of Physics: 2003; Vol. 82, p 4140.

(15) Coleman, J. N.; Cadek, M.; Blake, R.; Nicolosi, V.; Ryan, K. P.; Belton, C.; Fonseca, A.; Nagy, J. B.; Gun'ko, Y. K.; Blau, W. J. High performance nanotube-reinforced plastics: Understanding the mechanism of strength increase. *Adv. Funct. Mater.* **2004**, *14* (8), 791−798.

(16) Zhu, J.; Peng, H.; Rodriguez-Macias, F.; Margrave, J. L.; Khabashesku, V. N.; Imam, A. M.; Lozano, K.; Barrera, E. V. Reinforcing epoxy polymer composites through covalent integration of functionalized nanotubes. *Adv. Funct. Mater.* **2004**, *14* (7), 643−648.

(17) Peng, B.; Locascio, M.; Zapol, P.; Li, S.; Mielke, S. L.; Schatz, G. C.; Espinosa, H. D. Measurements of near-ultimate strength for multiwalled carbon nanotubes and irradiation-induced crosslinking improvements. *Nat. Nano* **2008**, *3* (10), 626−631.

(18) Fonseca, A. F.; Borders, T.; Baughman, R. H.; Cho, K. Load transfer between cross-linked walls of a carbon nanotube. *Phys. Rev. B* **2010**, *81* (4), 045429.

(19) Byrne, E. M.; McCarthy, M. A.; Xia, Z.; Curtin, W. A. Multiwall nanotubes can be stronger than single wall nanotubes and implications for nanocomposite design. *Phys. Rev. Lett.* **2009**, *103* (4), 045502.

(20) Fourches, D.; Pu, D.; Tassa, C.; Weissleder, R.; Shaw, S. Y.; Mumper, R. J.; Tropsha, A. Quantitative nanostructure activity relationship modeling. *ACS Nano* **2012**, *4* (10), 5703−5712.

(21) Burello, E.; Worth, A. P. QSAR modeling of nanomaterials. *Wiley Interdiscip. Rev.: Nanomed. Nanobiotechnol.* **2011**, *3* (3), 298−306.

(22) Puzyn, T.; Rasulev, B.; Gajewicz, A.; Hu, X.; Dasari, T. P.; Michalkova, A.; Hwang, H.-M.; Toropov, A.; Leszczynska, D.; Leszczynski, J. Using nano-QSAR to predict the cytotoxicity of metal oxide nanoparticles. *Nat. Nano* **2011**, *6* (3), 175−178.

(23) Puzyn, T.; Gajewicz, A.; Leszczynska, D.; Leszczynski, J.; Cronin, M. T. Nanomaterials − the Next Great Challenge for QSAR Modelers Recent Advances in QSAR Studies. Springer: Netherlands: 2012; Vol. 8, pp 383−409.

(24) Stuart, S. J.; Tutein, A. B.; Harrison, J. A. A reactive potential for hydrocarbons with intermolecular interactions. *J. Chem. Phys.* **2000**, *112* (14), 6472−6486.

(25) Brenner, D. W.; Shenderova, O. A.; Harrison, J. A.; Stuart, S. J.; Ni, B.; Sinnott, S. B. A second-generation reactive empirical bond order (REBO) potential energy expression for hydrocarbons. *J. Phys.: Condens. Matter* **2002**, *14* (4), 783−802.

(26) Shenderova, O. A.; Brenner, D. W.; Omeltchenko, A.; Su, X.; Yang, L. H. Atomistic modeling of the fracture of polycrystalline diamond. *Phys. Rev. B* **2000**, *61* (6), 3877−3888.

(27) Wei, C. Y.; Cho, K. J.; Srivastava, D. Tensile strength of carbon nanotubes under realistic temperature and strain rate. *Phys. Rev. B* **2003**, *67* (11), 115407.

(28) Swope, W. C.; Andersen, H. C.; Berens, P. H.; Wilson, K. R. A computer simulation method for the calculation of equilibrium constants for the formation of physical clusters of molecules: Application to small water clusters. *J. Chem. Phys.* **1982**, *76* (1), 637−649.

(29) Berendsen, H. J. C.; Postma, J. P. M.; van Gunsteren, W. F.; DiNola, A.; Haak, J. R. Molecular dynamics with coupling to an external bath. *J. Chem. Phys.* **1984**, *81* (8), 3684−3690.

(30) Srivastava, D.; Wei, C.; Cho, K. Nanomechanics of carbon nanotubes and composites. *Appl. Mech. Rev.* **2003**, *56* (2), 215−230.

(31) Todeschini, R.; Consonni, V. *Handbook of Molecular Descriptors*; Wiley-VCH: 2000; Vol. 11.

(32) Lipinski, C. A.; Lombardo, F.; Dominy, B. W.; Feeney, P. J. Experimental and computational approaches to estimate solubility and permeability in drug discovery and development settings. *Adv. Drug Delivery Rev.* **1997**, *23* (1−3), 3−25.

(33) Rajan, K. Materials informatics. *Mater. Today* **2005**, *8* (10), 38−45.

(34) Jancar, J.; Douglas, J. F.; Starr, F. W.; Kumar, S. K.; Cassagnau, P.; Lesser, A. J.; Sternstein, S. S.; Buehler, M. J. Current issues in research on structure-property relationships in polymer nano-composites. *Polymer* **2010**, *51* (15), 3321−3343.

(35) Tropsha, A.; Gramatica, P.; Gombar, V. K. The importance of being earnest: Validation is the absolute essential for successful application and interpretation of QSPR models. *QSAR Comb. Sci.* **2003**, *22* (1), 69−77.

(36) Krishnamoorti, R.; Vaia, R. A. Polymer nanocomposites. *J. Polym. Sci., Part B: Polym. Phys.* **2007**, *45* (24), 3252−3256.

(37) Gadzuric, S.; Suh, C.; Gaune-Escard, M.; Rajan, K. Extracting information from the molten salt database. *Metall. Mater. Trans. A* **2006**, *37* (12), 3411−3414.

(38) Srinivasan, S.; Rajan, K. Property phase diagrams for compound semiconductors through data mining. *Materials* **2013**, *6* (1), 279−290.

(39) Gasteiger, J.; Engel, T. *Chemoinformatics*; Wiley-VCH: 2003.

(40) Huang, C. Data fusion in scientific data mining. Ph.D. dissertation, Rensselaer Polytechnic Institute, Troy, NY, 2009.

(41) Bi, J.; Bennett, K.; Embrechts, M.; Breneman, C.; Song, M. Dimensionality reduction via sparse support vector machines. *J. Mach. Learn. Res.* **2003**, *3*, 1229−1243.

(42) Chambers, J. M.; Cleveland, W. S.; Kleiner, B.; Turkey, P. A. *Graphical Methods for Data Analysis*; Wadsworth: Belmont, Ca, 1983.

(43) Zhou, G.; Duan, W.; Gu, B. First-principles study on morphology and mechanical properties of single-walled carbon nanotube. *Chem. Phys. Lett.* **2001**, *333* (5), 344−349.

(44) Krishnan, A.; Dujardin, E.; Ebbesen, T. W.; Yianilos, P. N.; Treacy, M. M. J. Young's modulus of single-walled nanotubes. *Phys. Rev. B* **1998**, *58* (20), 14013.

(45) Sánchez-Portal, D.; Artacho, E.; Soler, J. M.; Rubio, A.; Ordejón, P. Ab initio structural, elastic, and vibrational properties of carbon nanotubes. *Phys. Rev. B* **1999**, *59* (19), 12678.

(46) Ozaki, T.; Iwasa, Y.; Mitani, T. Stiffness of single-walled carbon nanotubes under large strain. *Phys. Rev. Lett.* **2000**, *84* (8), 1712.

(47) Tunvir, K.; Nahm, S. H.; Kim, A.; Lee, H. J. Mechanical properties of carbon nanotubes with randomly distributed vacancy defects. *J. Korean Phys. Soc.* **2007**, *51* (6), 1940−1947.

(48) Haskins, R. W.; Maier, R. S.; Ebeling, R. M.; Marsh, C. P.; Majure, D. L.; Bednar, A. J.; Welch, C. R.; Barker, B. C.; Wu, D. T. Tight-binding molecular dynamics study of the role of defects on carbon nanotube moduli and failure. *J. Chem. Phys.* **2007**, *127* (7).

(49) Jeng, Y. R.; Tsai, P. C.; Fang, T. H. Effects of temperature and vacancy defects on tensile deformation of single-walled carbon nanotubes. *J. Phys. Chem. Solids* **2004**, *65* (11), 1849−1856.

(50) Sammalkorpi, M.; Krasheninnikov, A.; Kuronen, A.; Nordlund, K.; Kaski, K. Mechanical properties of carbon nanotubes with vacancies and related defects. *Phys. Rev. B* **2004**, *70*, 24.

(51) Mielke, S. L.; Troya, D.; Zhang, S.; Li, J. L.; Xiao, S. P.; Car, R.; Ruoff, R. S.; Schatz, G. C.; Belytschko, T. The role of vacancy defects and holes in the fracture of carbon nanotubes. *Chem. Phys. Lett.* **2004**, *390* (4−6), 413−420.

(52) Zhang, S. L.; Mielke, S. L.; Khare, R.; Troya, D.; Ruoff, R. S.; Schatz, G. C.; Belytschko, T. Mechanics of defects in carbon nanotubes: Atomistic and multiscale simulations. *Phys. Rev. B* **2005**, *71* (11).

(53) Vodenitcharova, T.; Zhang, L. C. Effective wall thickness of a single-walled carbon nanotube. *Phys. Rev. B* **2003**, *68* (16), 165401.

(54) Mylvaganam, K.; Zhang, L. C. Important issues in a molecular dynamics simulation for characterising the mechanical properties of carbon nanotubes. *Carbon* **2004**, *42* (10), 2025−2032.

(55) Yakobson, B. I.; Brabec, C. J.; Bernholc, J. Nanomechanics of carbon tubes: Instabilities beyond linear response. *Phys. Rev. Lett.* **1996**, *76* (14), 2511.

(56) Gupta, S.; Dharamvir, K.; Jindal, V. K. Elastic moduli of single-walled carbon nanotubes and their ropes. *Phys. Rev. B* **2005**, *72* (16), 165428.

(57) Popov, V. N.; Van Doren, V. E.; Balkanski, M. Elastic properties of single-walled carbon nanotubes. *Phys. Rev. B* **2000**, *61* (4), 3078.

(58) Lu, J. P. Elastic properties of carbon nanotubes and nanoropes. *Phys. Rev. Lett.* **1997**, *79* (7), 1297.

(59) Dereli, G.; Ozdogan, C. Structural stability and energetics of single-walled carbon nanotubes under uniaxial strain. *Phys. Rev. B* **2003**, *67* (3).

(60) Dereli, G.; Sangu, B. Temperature dependence of the tensile properties of single-walled carbon nanotubes: O(N) tight-binding molecular-dynamics simulations. *Phys. Rev. B* **2007**, *75* (18), 184104.

(61) Sun, X.; Zhao, W. Prediction of stiffness and strength of single-walled carbon nanotubes by molecular-mechanics based finite element approach. *Mater. Sci. Eng., A* **2005**, *390* (1−2), 366−371.

(62) Zhao, P.; Shi, G. Study of Poisson Ratios of Single-Walled Carbon Nanotubes based on an Improved Molecular Structural Mechanics Model. *CMC: Comput., Mater. Continua* **2011**, *22* (2), 147−168.

(63) Golbraikh, A.; Tropsha, A. Beware of q2! *J. Mol. Graphics Modell.* **2002**, *20* (4), 269−276.

(64) Chang, T.; Gao, H. Size-dependent elastic properties of a single-walled carbon nanotube via a molecular mechanics model. *J. Mech. Phys. Solids* **2003**, *51* (6), 1059−1074.

(65) Tienchong, C.; Jingyan, G.; Xingming, G., Chirality- and size-dependent elastic properties of single-walled carbon nanotubes. In *Applied Physics Letters*; American Institute of Physics: 2005; Vol. 87, p 251929.

(66) Iwasaki, Y.; Nakamiya, T.; Kozai, R.; Mitsugi, F.; Ikegami, T.; Elleithy, K.; Sobh, T.; Iskander, M.; Kapila, V.; Karim, M. A.; Mahmood, A. An Automatic Measurement Algorithm for the Diameters of Carbon Nanotubes by Using Image Processing. *Technological Developments in Networking, Education and Automation*; Springer: Netherlands: pp 275−280.

(67) Hernandez, E.; Goze, C.; Bernier, P.; Rubio, A. Elastic properties of single-wall nanotubes. *Appl. Phys. A: Mater. Sci. Process.* **1999**, *68* (3), 287−292.

(68) Mori, H.; Hirai, Y.; Ogata, S.; Akita, S.; Nakayama, Y. Chirality dependence of mechanical properties of single-walled carbon nanotubes under axial tensile strain. *Jpn. J. Appl. Phys.* **2005**, *44* (42), 1307−1309.

(69) Jiang, H.; Zhang, P.; Liu, B.; Huang, Y.; Geubelle, P. H.; Gao, H.; Hwang, K. C. The effect of nanotube radius on the constitutive model for carbon nanotubes. *Comput. Mater. Sci.* **2003**, *28* (3−4), 429−442.

(70) Gao, M.; Zuo, J. M.; Twesten, R. D.; Petrov, I.; Nagahara, L. A.; Zhang, R. Structure determination of individual single-wall carbon nanotubes by nanoarea electron diffraction. *Appl. Phys. Lett.* **2003**, *82* (16), 2703−2705.

(71) Deniz, H.; Derbakova, A.; Qin, L.-C. A systematic procedure for determining the chiral indices of multi-walled carbon nanotubes using electron diffraction - each and every shell. *Ultramicroscopy* **2010**, *111* (1), 66−72.

(72) Odom, T. W.; Huang, J.-L.; Kim, P.; Lieber, C. M. Atomic structure and electronic properties of single-walled carbon nanotubes. *Nature* **1998**, *391* (6662), 62−64.

(73) Dresselhaus, M. S.; Jorio, A.; Souza Filho, A. G.; Saito, R. Visualizing individual nitrogen dopants in monolayer graphene. *Science* **2011**, *333* (6045), 999−1003.

(74) Suzuki, S.; Hibino, H. Characterization of doped single-wall carbon nanotubes by Raman spectroscopy. *Carbon* **2011**, *49* (7), 2264−2272.

(75) Zhang, Z. Q.; et al. Mechanical properties of functionalized carbon nanotubes. *Nanotechnology* **2008**, *19* (39), 395702.

(76) Wang, S. Optimum degree of functionalization for carbon nanotubes. *Curr. Appl. Phys.* **2009**, *9* (5), 1146−1150.

(77) Kuang, Y. D.; He, X. Q. Young's moduli of functionalized single-wall carbon nanotubes under tensile loading. *Compos. Sci. Technol.* **2009**, *69* (2), 169−175.

(78) Namilae, S.; Chandra, N.; Shet, C. Mechanical behavior of functionalized nanotubes. *Chem. Phys. Lett.* **2004**, *387* (4−6), 247−252.

(79) Coto, B.; Antia, I.; Blanco, M.; Martinez-de-Arenaza, I.; Meaurio, E.; Barriga, J.; Sarasua, J.-R. Molecular dynamics study of the influence of functionalization on the elastic properties of single and multiwall carbon nanotubes. *Comput. Mater. Sci.* **2010**, *50* (12), 3417−3424.

(80) Deng, L.; Eichhorn, S. J.; Kao, C.-C.; Young, R. J. The effective Young's modulus of carbon nanotubes in composites. *ACS Appl. Mater. Interfaces* **2011**, *3* (2), 433−440.

(81) Hou, P.-X.; Liu, C.; Cheng, H.-M. Purification of carbon nanotubes. *Carbon* **2008**, *46* (15), 2003−2025.

(82) Chiang, I. W.; Brinson, B. E.; Huang, A. Y.; Willis, P. A.; Bronikowski, M. J.; Margrave, J. L.; Smalley, R. E.; Hauge, R. H. Purification and characterization of single-wall carbon nanotubes (SWNTs) obtained from the gas-phase decomposition of CO (HiPco process). *J. Phys. Chem. B* **2001**, *105* (35), 8297−8301.

(83) Lee, C.; Wei, X.; Kysar, J. W.; Hone, J. Measurement of the elastic properties and intrinsic strength of monolayer graphene. *Science* **2008**, *321* (5887), 385−388.

(84) Suk, J. W.; Piner, R. D.; An, J.; Ruoff, R. S. Mechanical properties of monolayer graphene oxide. *ACS Nano* **2010**, *4* (11), 6557−6564.

(85) Paci, J. T.; Belytschko, T.; Schatz, G. C. Computational studies of the structure, behavior upon heating, and mechanical properties of graphite oxide. *J. Phys. Chem. C* **2007**, *111* (49), 18099−18111.

(86) Mkhoyan, K. A.; Contryman, A. W.; Silcox, J.; Stewart, D. A.; Eda, G.; Mattevi, C.; Miller, S.; Chhowalla, M. Atomic and electronic structure of graphene-oxide. *Nano Lett.* **2009**, *9* (3), 1058−1063.

(87) Ossi, L.; et al. Characterization of ion-irradiation-induced defects in multi-walled carbon nanotubes. *New J. Phys.* **2011**, *13* (7), 073004.